Influence of the Cathodic Binder on CO_2 Electroreduction to Formic Acid in a Three-Compartment Electrolyzer

Konstantin von Foerster,* Sergio Sanz,* Krzysztof Dzięcioł, Urbain Nzotcha, Bastian Rutjens, Bernhard Schmid, Hermann Tempel and Rüdiger-A. Eichel

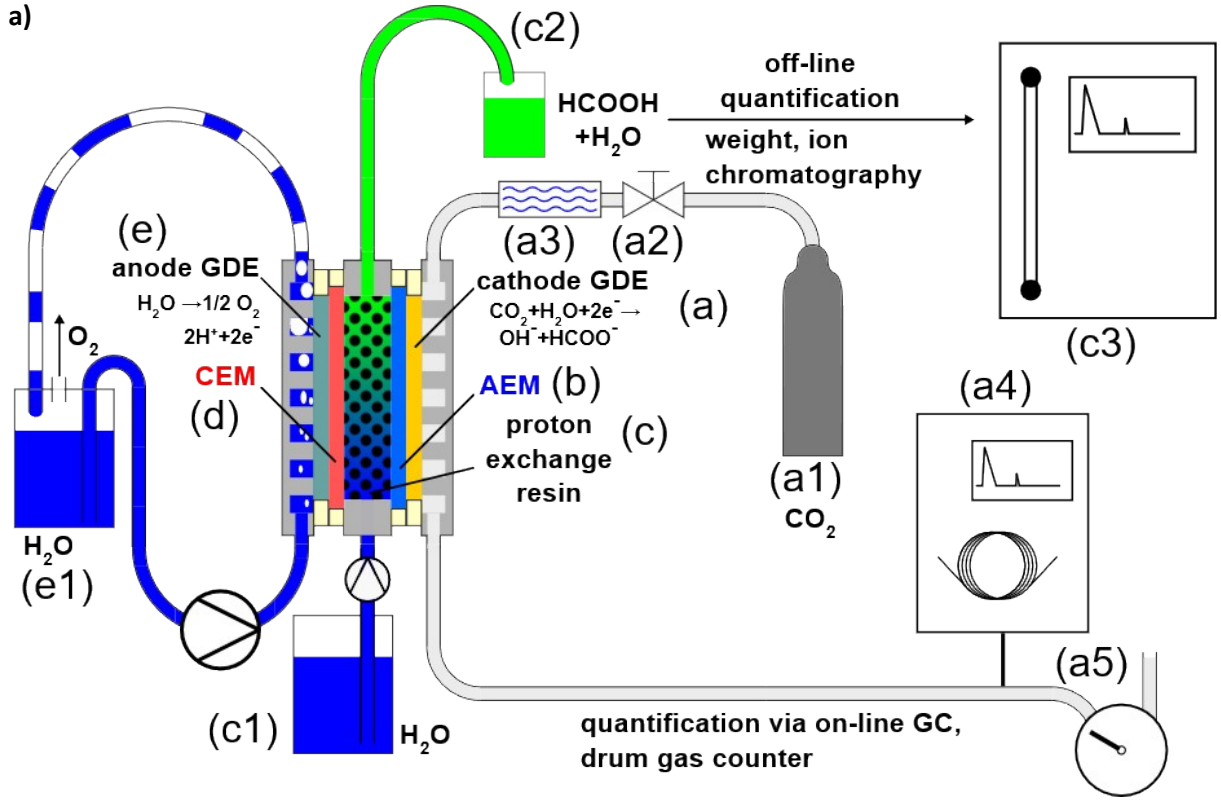

Figure S1. Schematic representation of the employed DFAP electrolyzer. Cathode (a): gaseous CO_2 (a1) passes a mass flow controller (a2) and a membrane humidifier (a3) before being fed to the cathodic GDE. The exhaust gas composition is quantified via in-line GC (a4), and the volume flow is measured via a drum gas counter (a5). An AEM (b) separates the cathode and the center compartment (c), which is filled with a proton exchange resin. Deionized water is fed to the center compartment in single pass mode (c1), and the product (c2) is quantified via ion chromatography (c3). A CEM (d) separates the center compartment and the anode (e). The anode is fed with deionized water (e.1) in a recirculation mode.

Binder load variation

Experiments using cathode GDEs fabricated with 6.25 mg of PVDF/HFP binder on 100 mg of Bi_2O_3 catalyst yielded unstable cell voltages, faradaic efficiencies to formic acid, and product concentration at 200 mA cm^{-2}. Since the use of cathodic PVDF/HFP binder in a DFAP reactor was not reported yet, a load variation study was performed, testing additionally 25 mg and 125 mg of PVDF/HFP per 100 mg of Bi_2O_3 (Figure S2). With a 25 mg load, stable operation was observed across all investigated current densities, even reaching as high as 750 mA cm^{-2}. At a binder load of 6.25 mg, unstable operation marked by fluctuating voltages and reduced selectivity was observed at 200 mA cm^{-2}. Current densities of 750 mA cm^{-2} could not be reached with this binder load. With a load of 125 mg of PVDF/HFP, low selectivity for formic acid, high potentials, and high energy consumption were observed at 200 mA cm^{-2}. A cell voltage increase over the course of the measurement indicates significant degradation. The limited current density with this load was 350 mA cm^{-2}, presenting low selectivity for formic acid and high voltages, which indicates significant transport limitation due to pore blockage by the binder. Hence, the optimal load of 25 mg was chosen for all measurements, purportedly striking a balance between suboptimal hydrophobicity and excessive pore blockage.

In a comparative experiment, a 25 mg load of PiperION binder per 100 mg of Bi_2O_3 yielded significantly increased cell voltages and specific energy consumptions, indicating transport limitations that are likely due to the higher hydrophilicity of ionomer binders compared to PVDF/HFP. Hence, an optimum load of 25 mg for PVDF/HFP and 6.25 mg for all ionomer binders was chosen as the

respective optimum load.

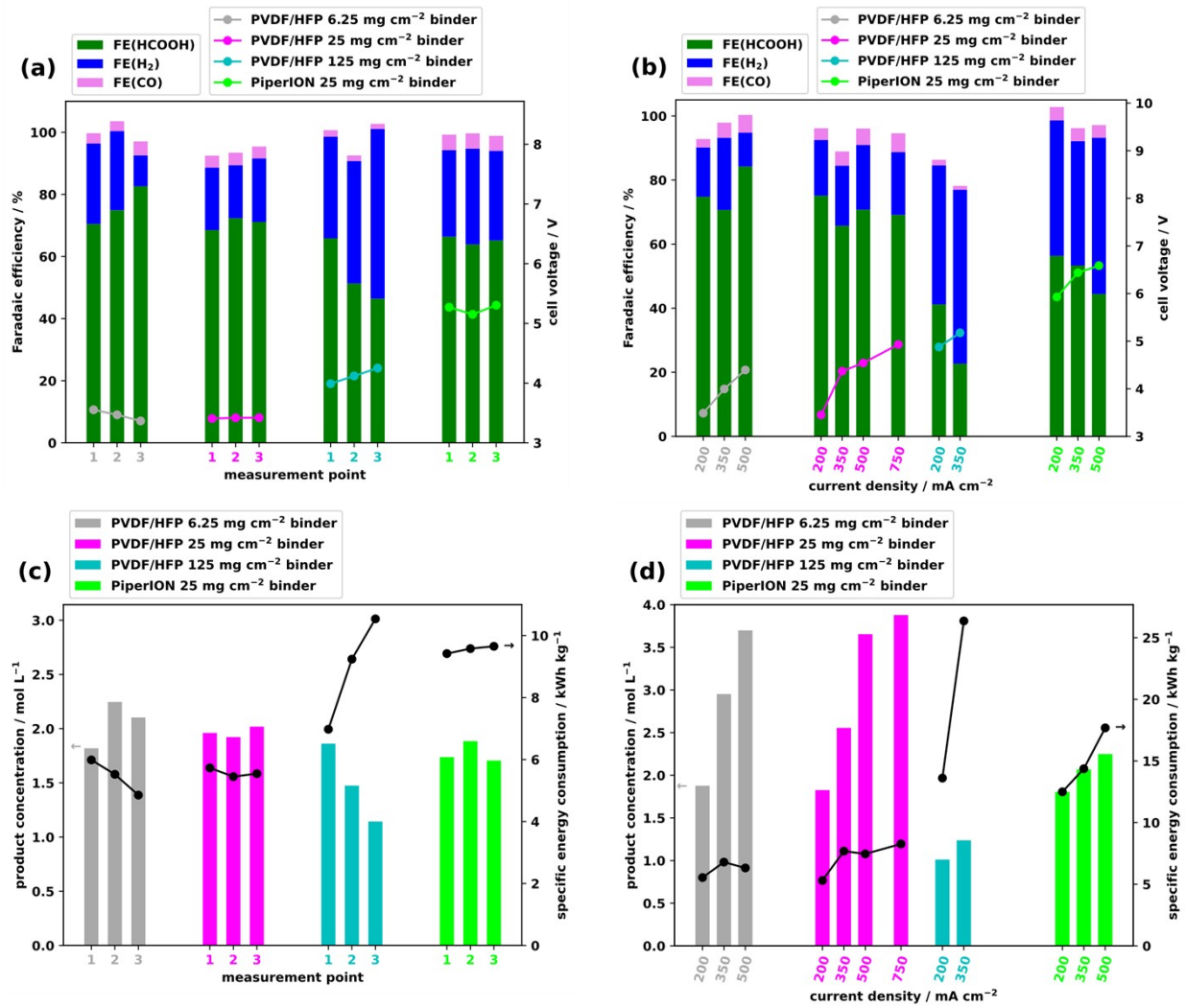

Figure S2. Key performance indicators (KPIs) using GDEs with different loads of PVDF/HFP binder and with an increased load of PiperION binder, using a 40 µm PiperION AEM: (a) Faradaic efficiency and cell voltage variation over 3 h measuring time (1 h interval) at 200 mA cm^{-2}, (b) Faradaic efficiency and cell voltage variation at different current densities (sampling after 30 min of stable cell operation), (c) formic acid concentration and energy consumption over 3 h measuring time (1 h interval) at 200 mA cm^{-2}, and (d) formic acid concentration and energy consumption at different current densities (sampling after 30 min of stable cell operation). The plotted data is listed in table S1.

Table S1. Overview of the operation parameters, faradaic efficiencies, cell voltage, specific energy consumption, and formic acid concentration of all values in Figure 2 in the article, with standard deviations. The results using Sustainion, PVDF/HFP, and Nafion as a cathode binder were obtained as averages from two values. Data from plotted results using the cathodic PiperION binder are averages from three measurements and were obtained from ref. 1, available under a CC-BY 4.0 license. Copyright 2024 B. Rutjens et al. Asterisks denote single-point measurements.

binder	current density [mA cm^{-2}]	measurement duration [h]	FE(HCOOH) [%]	FE(H_2) [%]	FE(CO) [%]	cell voltage [V]	specific energy consumption [kWh kg^{-1}]	*c*(HCOOH) [M]
PiperION[1]	200[1]	1[1]	73±7.6[1]	17±4.7[1]	4.4±0.26[1]	4.0±0.31[1]	6.4±1.1[1]	2.2±0.52[1]
PiperION[1]	200[1]	1[1]	77±7.1[1]	16±6.5[1]	4.5±0.35[1]	3.9±0.33[1]	5.9±0.56[1]	2.3±0.43[1]
PiperION[1]	200[1]	1[1]	75±9.7[1]	16±6.2[1]	4.5±0.37[1]	3.8±0.37[1]	6.0±0.53[1]	2.3±0.56[1]
PiperION[1]	500[1]	0.5[1]	69±4.1[1]	27±7.5[1]	5.1±0.84[1]	4.9±0.36[1]	8.3±0.62[1]	4.0±1.6[1]
PiperION[1]	350[1]	0.5[1]	65±11[1]	24±7.7[1]	4.8±0.68[1]	4.4±0.35[1]	8.0±0.99[1]	3.6±1.7[1]
PiperION[1]	200[1]	0.5[1]	67±3.9[1]	22±9.8[1]	4.4±0.45[1]	3.9±0.24[1]	6.7±0.58[1]	2.4±1.2[1]
Sustainion	200	1	62±22	28±19	2.8±0.53	3.7±0.17	7.3±2.9	1.8±0.71
Sustainion	200	1	67±19	24±11	2.9±0.02	3.7±0.12	6.5±2.1	2.0±0.62
Sustainion	200	1	64±12	19±6.7	3.1±0.22	3.7±0.07	6.7±1.3	1.9±0.47
Sustainion	500	0.5	62*	12*	6.1*	4.9*	9.1*	3.1*
Sustainion	350	0.5	65±0.89	17±8.0	4.2±1.6	4.3±0.07	7.6±0.22	3.1±0.15
Sustainion	200	0.5	65±6.1	15±7.4	4.1±0.37	3.6±0.05	6.3±0.67	2.0±0.22
PVDF/HFP	200	1	69±0.92	20±2.4	3.8±0.25	3.4±0.05	5.7±0.01	2.0±0.05
PVDF/HFP	200	1	72±0.98	17±0.52	4.0±0.24	3.4±0.04	5.4±0.13	1.9±0.02
PVDF/HFP	200	1	71±2.7	20±4.3	3.8±0.18	3.4±0.05	5.5±0.13	2.0±0.36
PVDF/HFP	750	0.5	69±1.4	20±1.5	5.8±0.29	4.9±0.20	8.3±0.17	3.9±0.30
PVDF/HFP	500	0.5	71±6.5	20±3.6	5.1±0.37	4.5±0.12	7.5±0.50	3.7±0.30
PVDF/HFP	350	0.5	66*	19*	4.4*	4.4*	7.7*	2.6*
PVDF/HFP	200	0.5	75±3.5	17±1.1	3.6±0.22	3.5±0.20	5.3±0.54	1.8±0.19
Nafion	200	1	69±11	10±3.8	5.8±1.1	3.9±0.15	6.6±0.78	2.1±0.36
Nafion	200	1	73±0.12	11±5.4	5.7±0.99	3.9±0.12	6.2±0.19	2.4±0.55
Nafion	200	1	72±8.9	11±3.4	6.2±0.64	3.9±0.11	6.3±0.61	2.2±0.37
Nafion	500	0.5	55*	32*	6.3*	5.3*	11*	2.4*
Nafion	350	0.5	71±2.2	17±8.1	6.0±0.91	5.4±0.13	8.9±0.48	2.5±0.85
Nafion	200	0.5	77±5.7	12±7.4	5.0±0.20	4.1±0.45	6.1±1.2	2.3±0.14
PVDF/HFP	200	1	70	26	3.3	3.6	6.0	1.8
6.25 mg per	200	1	75	25	3.2	3.5	5.5	2.2
100 mg of	200	1	83	10	4.5	3.4	4.9	2.1
catalyst	500	0.5	84	11	5.5	4.4	6.3	3.7
	350	0.5	71	23	4.7	4.0	6.8	3.0
	200	0.5	75	15	2.7	3.5	5.5	2.9
PVDF/HFP	200	1	66	33	2.1	4.0	7.0	1.9
125 mg per	200	1	51	39	1.8	4.1	9.2	1.5
100 mg of	200	1	46	55	1.6	4.3	11	1.1
catalyst	350	0.5	23	54	1.2	5.2	26	1.3
	200	0.5	41	43	1.7	4.9	14	1.0
PiperION	200	1	66	28	5.0	5.3	9.4	1.7
25 mg per	200	1	64	31	4.9	5.2	9.6	1.9
100 mg of	200	1	65	29	4.8	5.3	9.7	1.7
catalyst	500	0.5	44	49	3.9	6.6	18	2.2
	350	0.5	53	39	4.0	6.4	14	2.1
	200	0.5	56	42	4.1	5.9	12	1.8

Amount of K^+ ions required to neutralize the Nafion binder

This calculation takes into account the approximate Nafion mass m and its equivalent weight EW_2 as well as the charge numbers of potassium and sulfonate z.

$$n_{K+} = \frac{z_{RSO_2OH}}{z_{K+}} \cdot \frac{m_{Nafion}}{EW}$$

$$n_{K+} = \frac{1}{1} \cdot \frac{6\,mg}{1100\,g\,mol^{-1}}$$

$$n_{K+} = 5.5\,\mu mol$$

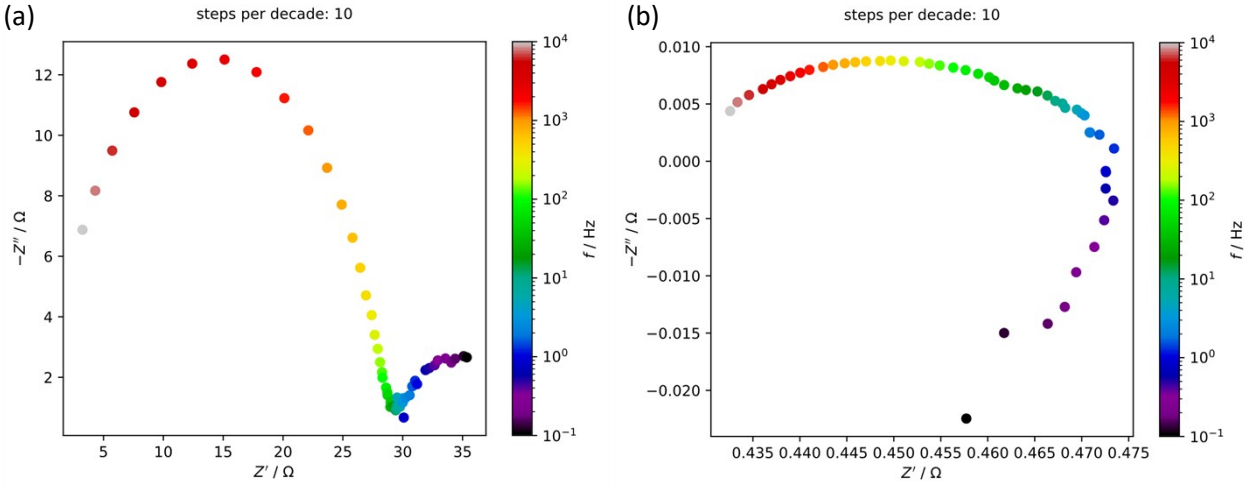

Figure S3. PEIS spectra of the DFAP electrolyzer with a PiperION AEM (non-preconditioned with KOH) and a PVDF/HFP-bound GDE. (a) At 4.2 V and 0.42 V amplitude before center compartment treatment with K_2SO_4 solution, and (b) at 5 V and 0.5 V amplitude after K_2SO_4 treatment.

Observation of potassium in the EDX mapping of a post-mortem GDE with PVDF/HFP binder

(a)

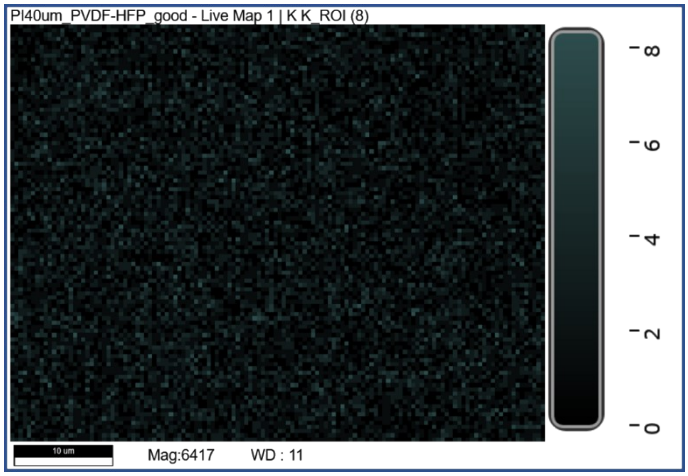

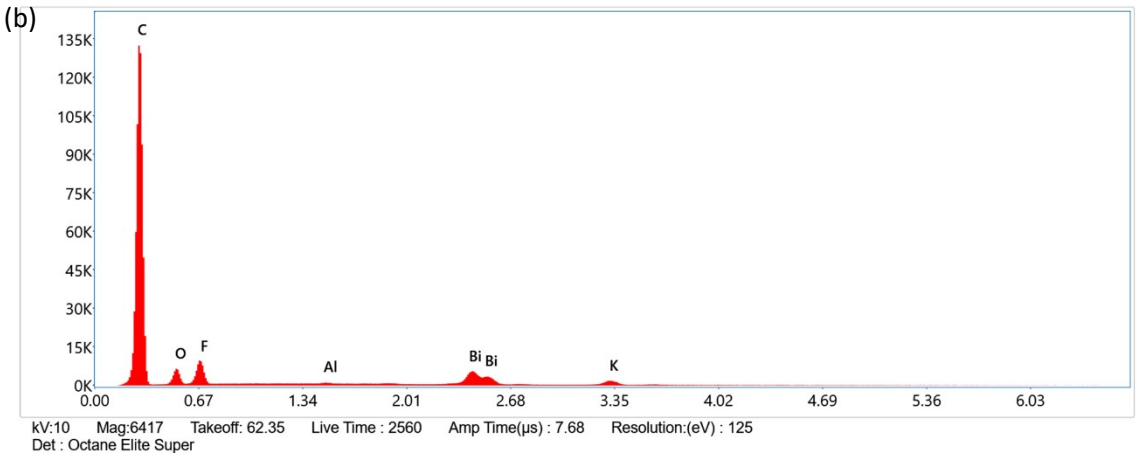

Figure S4. (a) EDS map of potassium of a post-mortem cross-section of a PVDF/HFP-bound GDE after operation with a PiperION AEM, corresponding to Figure 5c in the article. (b) Energy distribution of all mapped X-rays with the corresponding elements assigned, displaying that potassium is reliably observed.

EDX spot measurement of crystalline high-intensity plaques on post-mortem GDE with PVDF/HFP binder

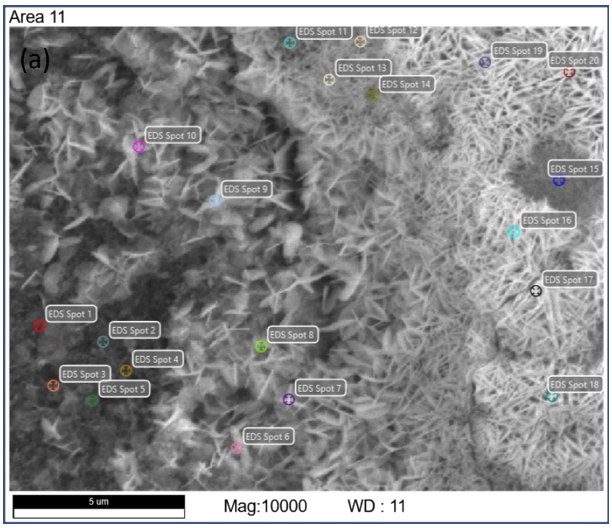

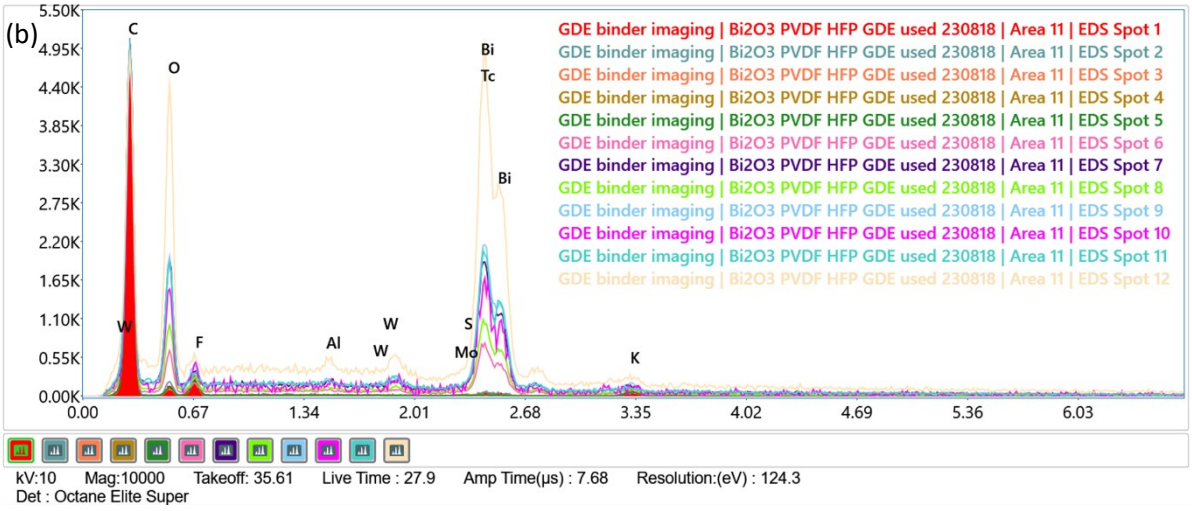

Figure S5. (a) SEM image at large magnification with marked EDS spot measurements and (b) corresponding energy histogram of

a post-mortem PVDF/HFP-bound GDE. The first five signals were recorded in the darker colored area, apart from the crystalline species (showing white color); these essentially displayed no counts in the energy region corresponding to Bi. In contrast, Bi is observed at the positions starting from 6, which were taken on the flake-shaped crystallite positions (showing white color). Therefore, the observed white flake-shaped crystallites represent the catalytically active species.

SEM cross-section images of pristine and post-mortem GDEs with all four employed binders

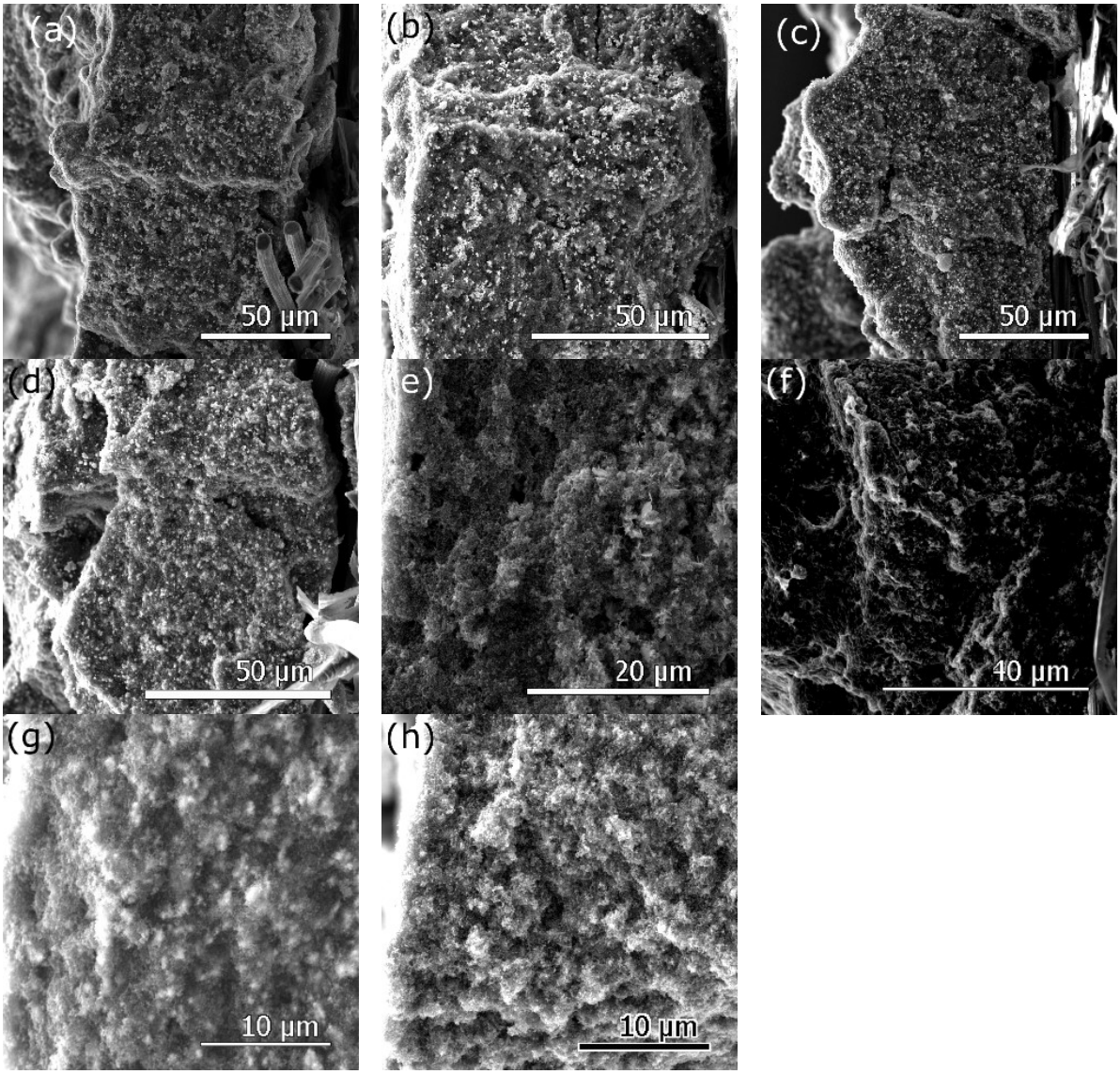

Figure S6. Cross-section SEM images of pristine GDEs fabricated with (a) PVDF/HFP, (b) Nafion, (c) Sustainion, and (d) PiperION binder and post-mortem GDEs fabricated with (e)PVDF/HFP, (f) Nafion, (g) Sustainion, and (h) PiperION binder.

Table S2. Parameters of the conducted XCT experiments.

Sample	Resolution [µm]	X-ray tube voltage [kV]	Exposure [s]	Number of projections
GDE	3.4	30	2	1600
GDE	0.68	40	6	1600
AEM	1.56	40	5	1600
AEM	0.68	70	10	1600

Determining layer thicknesses from XCT images

The thickness determination algorithm, implemented in MATLAB (The MathWorks, Inc., Natick, US), first selects the voxels of interest, *i.e.*, those that make up the layer, via thresholding. Subsequently, domains containing catalyst are removed via the exclusion of high intensity voxels. After thresholding, morphological closing operation is performed to remove the internal porosity. Resultant binary image is skeletonized (MATLAB's bwskel), providing voxels equidistant from both sides of the membranes. The Euclidean distance transform (MATLAB's bwdist) is computed on an inverted binary image (background voxels = 1, layer's voxels = 0). Finally, the distance transform is masked by skeleton through element-wise multiplication, so that distance values are retained only along the skeleton voxels. Because the skeleton is centred, the local thickness at each skeleton voxel is exactly twice the corresponding masked distance value. The pseudo-code of complete procedure is presented in Algorithm 1.

Algorithm 1
Input: 3D grayscale volume V, Thresholds Th_low, Th_high

1. I_layer ← (V ≥ Th_low) // binarize to select whole catalyst layer
2. I ← I_layer ∧ (V < Th_high) // remove high-intensity catalyst particles
3. I ← MorphologicalClosing(I)
4. S ← Skeletonize(I)
5. D ← EuclideanDistanceTransform(¬I)
6. T_skeleton ← 2 × (D ⊙ S)

Output: Thickness map T_skeleton

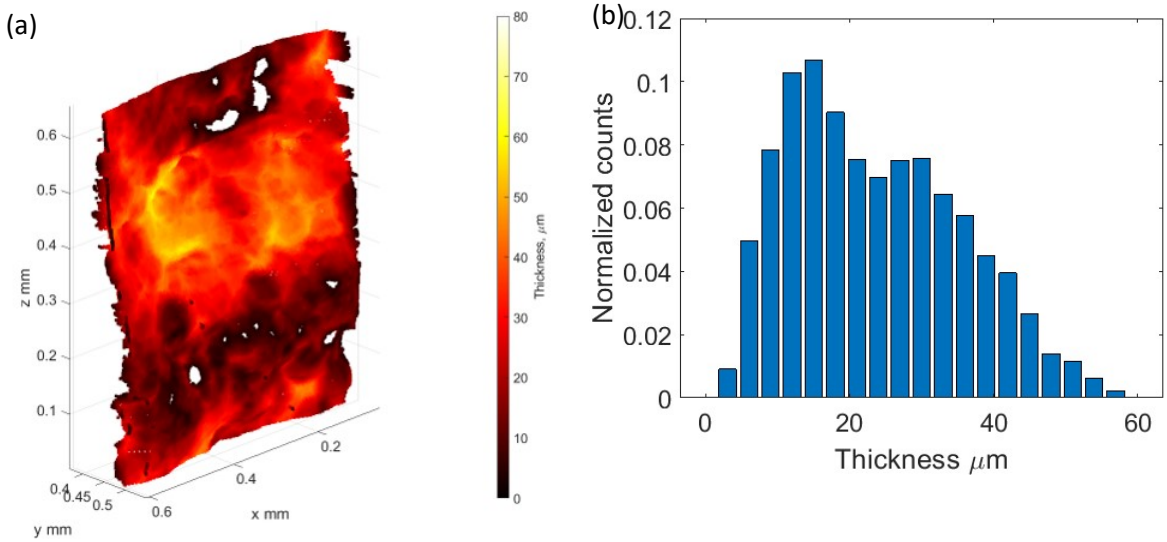

Figure S7. (a) Thickness of the catalyst-depleted layer of the CL on a section of the GDE with PVDF/HFP binder. (b) Corresponding thickness histogram.

Potassium demand of the catalyst layer and transport rates across the AEM

The catalyst layer ranged from 40 to 80 µm thick, varying due to differences in agglomerate size, packing densities, and other structural factors. Considering the active surface area of 5 cm^2, this corresponds to a total CL volume of 0.02-0.04 cm^3 or 20-40 µL. Hence, to obtain a K^+ concentration of

1M at the cathode, migration of 2-4 µmol of ions is required, equivalent to the K^+ content of 20-40 µL of the 0.5 M K_2SO_4 activation solution with $c(K^+) = 2 \cdot 0.5\ mol\ L^{-1}$. Assuming activation to occur over 50 min as is the case in Figure 4b in the article, this requires average K^+ migration rates between $\frac{20\ \mu L \cdot 1\ mol\ L^{-1}}{3000\ s\ \cdot 5\ cm^2} = 1.33\ nmol\ s^{-1} cm^{-2}$ and $2.67\ nmol\ s^{-1} cm^{-2}$.

In comparison, the number of migrating charges per area follows the correlation $\frac{\dot{n}_{electrons}}{A} = \frac{j}{F}$. At 200 mA cm^{-2}, this corresponds to $2.1\ \mu mol\ s^{-1} cm^{-2}$ which is by three orders of magnitude larger. As PiperION AEMs support even higher current densities, K^+ migration in these amounts would be possible even if cation transference numbers were around 1000 ppm or even lower.

Hypothetical required catalyst activity without cathodic ionic conduction

Assuming no ionic conduction inside the catalyst layer with a thickness d_{CL}, the amount of active catalyst per geometric area $m_{cat,active}$ is assumed to be the amount that can be in direct contact with the AEM, i.e., the amount inside the top layer with a thickness of the average catalyst particle size d_{cat}. The amount of catalyst inside that layer corresponds to the total catalyst mass multiplied by d_{cat}/d_{CL}. Referencing this to the maximum total current density and FE(HCOOH), an apparent catalyst activity $i_{0,apparent,assumption}$ is obtained, which can be compared to a reference activity $i_{0,apparent} = 583.9\ A\ g^{-1}$ from the literature.[3]

$$m_{cat,\ active} = m_{cat,\ total} \cdot \frac{d_{cat}}{d_{CL}}$$

$$m_{cat,\ active} = 4\ mg\ cm^{-2} \cdot \frac{100\ nm}{60\ \mu m} = 6.7 \cdot 10^{-3}\ mg\ cm^{-2}$$

$$i_{0,apparent,assumption} = \frac{j_{max} \cdot FE(HCOOH)}{m_{cat,active}}$$

$$i_{0,apparent,assumption} = \frac{750\ mA\ cm^{-2} \cdot 69\%}{6.7 \cdot 10^{-3}\ mg\ cm^{-2}} = 7.76 \cdot 10^3\ A\ g^{-1}$$

This is by a factor of 13.3 larger than the reference value of 583.9 A g^{-1}. Hence, we suspect that more than the catalyst inside this top layer needs to be active, which requires the conduction of anions towards the AEM from catalyst particles at larger distances to the AEM.

Model for volume current support limited by Ohmic resistance and catalyst activity

ΔU	maximum cathodic cell voltage drop [V]
I	current [A]
j	current density [mA cm^{-2}]
l	layer thickness [m]
ρ	specific resistance [Ω cm]
A	geometric electrolysis area [cm^2]
m_{cat}	catalyst mass [g]
$m_{spec,cat}$	area-specific catalyst load [g cm^{-2}]
$i_{0,apparent}$	highest reported CO_2-to-HCOOH activity of a Bi-based catalyst [A g^{-1}]

$\iota_{0,apparent}$	Local current change inside the catalyst layer [A m^{-1}]
d_{layer}	catalyst layer thickness [m]

This model aims at determining the minimum expectable Ohmic voltage losses over the cathodic electrolyte film at a given current density, assuming that the catalyst is either completely active if the Ohmic voltage loss allows to reach it or is inactive if the distance between the catalyst and the AEM is larger than the voltage allows.

$$\frac{d\Delta U}{dl} = \frac{\rho}{A} I(l)$$
$$\Delta U = \int_0^l \frac{\rho}{A} I(x) dx \qquad 1$$

For regular conduction, integration gives Ohm's law as $I(l) = const.$, which is not given here. Rather, $I(x)$ increases towards the CL|AEM interface as the local catalyst activity generates anions. The increase is related to the local current change $\iota_{0,apparent}$. $\iota_{0,apparent}$ is derived from the catalyst activity, using the highest apparently possible current density $i_{0,apparent}$ from the literature for a very active Bi-based catalyst (Bi nanosheets, [3]) and the area-specific catalyst load $m_{spec,cat}$.

$$\frac{d\Delta U}{dl} = \frac{\rho}{A} I(l)$$
$$i_{0,apparent} = \frac{I}{m_{cat}}$$

$$I = i_{0,apparent} \cdot m_{cat}$$
$$j_{0,apparent} = i_{0,apparent} \cdot \frac{m_{cat}}{A}$$

$$j_{0,apparent} = i_{0,apparent} \cdot m_{spec,cat}$$

Assuming a homogeneously distributed catalyst, the apparent specific limiting current density per d span $\iota_{0,apparent}$ can be calculated.

$$\iota_{0,apparent} = \frac{i_{0,apparent} \cdot m_{cat}}{d_{layer}} \qquad 2$$
$$\iota_{0,apparent} = \frac{i_{0,apparent} \cdot m_{spec,cat} \cdot A}{d_{layer}} \qquad 3$$

Here, the catalyst is assumed to be completely active according to $\iota_{0,apparent}$ close to the AEM and completely inactive at larger distance. While this assumption neglects the increase of the reaction overpotential due to transport and kinetic limitations near the catalyst particle, it gives a lower limit for the Ohmic transport losses inside the CL.[1] It leads to a linear connection between $I(x)$ and x.

$$I(x) = \iota_{0,apparent} \cdot x \qquad 4$$

[1] This is because such an overpotential would cause a slower local increase of the current towards the AEM. With the constraints that the slope of $I(x_{max})$ must be between zero and $\iota_{0,apparent}$, a linear would always increase the distance of the deeper active catalyst to the AEM|CL interface.

$I_{max} \equiv I$ represents the applied current. It allows to get the maximum depth at which catalyst activity is observed.

$$x_{max} = \frac{I}{\iota_{0,apparent}} \quad (5)$$

For reasons of simplicity, the x axis is chosen to start at 0 at a distance of x_{max} inside the CL, x_{max} being the location of the CL|AEM interface.

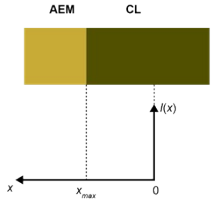

Using this coordinate system, equations 2, 4 and 5 are inserted into equation 1.

$$\Delta U(x_{max}) = \int_0^{x_{max}} \frac{\rho}{A} \iota_{0,apparent} \cdot x dx \quad (6)$$

$$\Delta U(x_{max}) = \left[\frac{\rho \iota_{0,apparent}}{2A} \cdot x^2 \right]_0^{x_{max}}$$

$$\Delta U(x_{max}) = \frac{\rho \iota_{0,apparent}}{2A} \cdot x_{max}^{\ 2}$$

$$\Delta U(I) = \frac{\rho}{2A \cdot \iota_{0,apparent}} \cdot I^2$$

$$\Delta U(j) = \frac{\rho \cdot A}{2\ \iota_{0,apparent}} \cdot j^2$$

$$\Delta U(j) = \frac{\rho \cdot d_{layer}}{2\ i_{0,apparent} \cdot m_{spec,cat}} \cdot j^2$$

At the maximum achievable current density, ΔU can be arbitrarily large. Hence, the equation is rearranged to give the current density as an argument of the available Ohmic overpotential budget.

$$j(\Delta U) = \sqrt{\frac{2\ i_{0,apparent} \cdot m_{spec,cat}}{\rho \cdot d_{layer}}} \cdot \sqrt{\Delta U} \quad (7)$$

if $j\ (\Delta\ U) < i_{0,apparent} \cdot m_{spec,cat}$:

else: $j(\Delta U) = i_{0,apparent} \cdot m_{spec,cat}$

Table S3. Overview of the operation parameters, faradaic efficiencies, cell voltage, specific energy consumption, formic acid concentration, and potassium ion concentration in the product of the 24 h measurement at 500 mA cm^{-2} (Figure 6a in the article). ICP-MS samples were measured threefold in a 1:20 dilution, blank concentration: <0.3 mg L^{-1}.
*1 autosampler got stuck, so both samples were collected in one vial.

measurement duration [h]	FE(HCOOH) [%]	FE(H_2) [%]	FE(CO) [%]	cell voltage [V]	specific energy consumption [kWh kg^{-1}]	*c*(HCOOH) [M]	*c*(K^+) center [mg L^{-1}]
4*1	67	20.0	5.36	4.90	8.82	3.32	2.83±0.06
2	73	22.6	5.16	4.92	8.16	3.22	1.5±0.1
2	72	21.0	5.43	4.95	8.34	3.60	1.09±0.03
2	69	25.4	5.07	4.94	8.64	3.42	0.94±0.09
2	73	21.9	5.49	4.95	8.18	3.46	1.56±0.05
2	71	21.1	5.33	4.91	8.37	3.81	0.6±0.2

2	80	18.6	5.21	4.94	7.49	3.51	0.90±0.07
2	74	22.3	5.15	4.89	8.05	3.71	1.57±0.05
2	74	18.9	5.31	4.92	8.05	3.42	<0,3
2	69	22.9	5.19	4.89	8.49	3.14	1.9±0.1
2	82	18.5	5.31	5.03	7.43	3.64	<0.3

Table S4. Overview of the operation parameters, faradaic efficiencies, cell voltage, specific energy consumption, formic acid concentration, and potassium ion concentration in the product of the 24 h measurement at 200 mA cm^{-2} (Figure 6b in the article). *1 compensation for 1 h of stabilisation time. *2 delayed sampling due to an autosampler malfunction.

measurement duration [h]	FE(HCOOH) [%]	FE(H_2) [%]	FE(CO) [%]	cell voltage [V]	specific energy consumption [kWh kg^{-1}]	*c*(HCOOH) [M]
2	82	15.1	4.6	3.53	5.13	2.32
2	77	19.7	4.3	3.54	5.49	2.26
2	76	21.2	4.5	3.69	5.77	2.19
2	74	22.4	4.4	3.67	5.87	2.22
2	69	23.4	4.3	3.63	6.23	2.23
2	79	22.6	4.2	3.56	5.41	2.27
2	71	25.4	4.3	3.76	6.34	2.16
2.5*1	66	26.0	3.9	3.61	6.49	2.01
2.5*1	73	26.4	4.0	3.57	5.87	2.18
3.056*2	71	27.3	4.0	3.58	6.04	2.19
1.944*2	69	24.1	3.3	3.64	6.26	2.13

Catalyst migration model – a more detailed description

Under reducing conditions, Bi_2O_3 is reduced to Bi(0) at the cathode.[4] This can, in turn, undergo cathodic corrosion by nascent hydrogen, forming BiH_3, which rapidly decays, producing Bi(0) into the cathodic electrolyte film.[5,6] However, this is unlikely to account for the long-range catalyst redistribution observed by micro-XCT and is only a minor contributing effect. Hence, we derived an explanatory qualitative model based on the cathode alkalinity involving catalyst dissolution, transport, and reprecipitation (Figure S8). Depending on the abundance of CO_2 and OH^-, the following species may coexist.

$$OH^- \xrightarrow{+CO_2} CO^{2-}_3, OH^- \xrightarrow{+CO_2} CO^{2-}_3, HCO^-_3 \xrightarrow{+CO_2} HCO^-_3, CO_2$$

The pH can stretch from strongly alkaline conditions in the presence of hydroxide ions to weakly acidic conditions for a CO_2-saturated bicarbonate electrolyte. Based on the evolution of CO and H_2 inside the catalyst layer and the consumption of CO_2 by reaction with hydroxide, the CO_2 concentration decreases towards the PiperION AEM (Figure S8a). Consequently, the depicted buffer systems lead to an increasing pH value towards the AEM (Figure S8b). As a result, the solubility of aqueous Bi^{III} species decreases towards the AEM (Figure S8c).[7] Arising from the solubility gradient, a net flux of Bi^{III} ions towards the AEM is predicted by Fick's first law of diffusion (Figure S8d), precipitating and accumulating at the CL|AEM interface (Figure S8e). Besides, the mobility of cationic Bi^{III} species is reduced at the AEM by its permselectivity against cation transport[8] and the opposition of cation movement across the AEM by electromigration. Under strongly alkaline conditions in the active region $[Bi(OH)_4]^{-}$ [7] could be formed and migrate towards the center compartment across the AEM. As the pH decreases within the AEM towards the center compartment, it would then precipitate as $Bi(OH)_3$ inside the AEM. Micro-XCT imaging (Figure 6c in the article) did not reveal any bismuth species inside the AEM, indicating that no bismuth transport occurred across the AEM. The restructuration of the catalyst

from the inner layers and its accumulation at the CL|AEM interface when using the PVDF/HFP binder in the GDE does not impair the eCO_2R-to-HCOOH performance within the duration of the experiments.

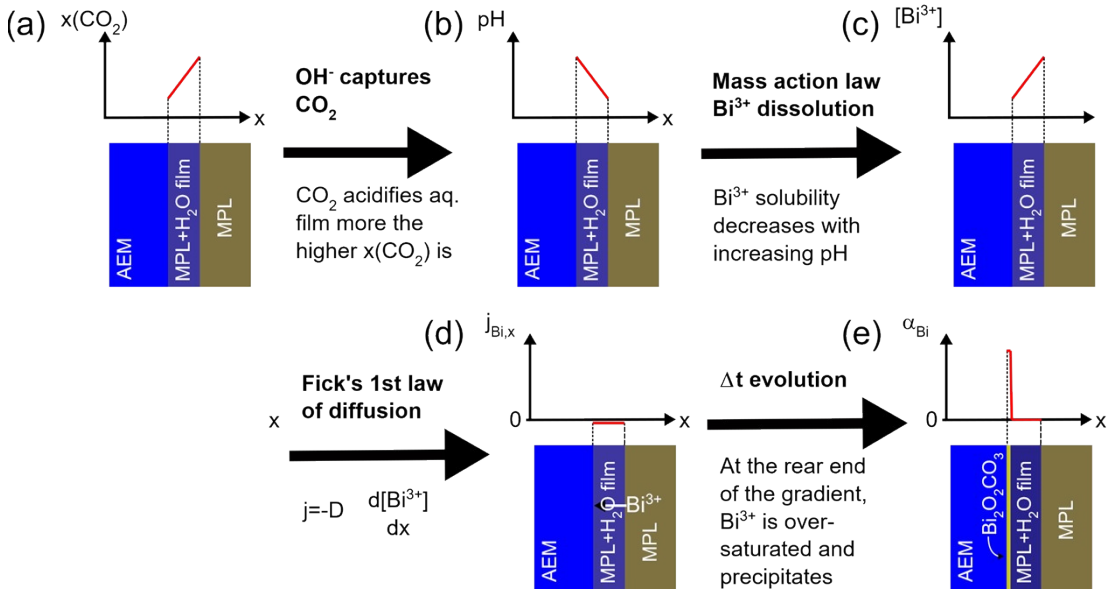

Figure S8. Qualitative model representation of processes that might lead to solubility-driven transport of Bi^{3+} ions in an aqueous film in the CL, based on the abundance of CO_2 (a), which influences the pH value inside the water film (b), and in turn, the Bi^{3+} solubility limit (c), and mass transport (d). The result is the accumulation of catalyst from the affected CL sections at the CL|AEM interface (e).

Table S5 Baseline assumptions for the operation of the hypothetical DFAP electrolyzer.

Item	Units	Value	Reference
Number of cells per stack	~	200	Assumed
Cell's electrode active area	m^2	0.6	Assumed
Plant total active area	m^2	3,600	Assumed
Plant capacity utilization factor (CUF)	%	75	Assumed
Single-pass CO_2 conversion efficiency	%	30	Assumed
Unreacted CO_2 recycling model	~	~	Amine-based system [9,10] PSA system from[11]
Formic acid purification model	~	~	Hybrid extraction-distillation[9,10] Azeotropic distillation[11]
Product losses during separation	%	3.0	Assumed
Process consumables as a percentage of total CapEx	%	2.0	Assumed
Average renewable energy cost	¢ kWh^{-1}	4.5	Average large renewable energy price
CO_2 cost	\$ $tonne^{-1}$	40	Assumed from [12]
Deionized water cost	\$ gal^{-1}	0.0054	Assumed from [13]
Membrane electrodes assembly life	hours	3,000	Assumed from [14,15]
Electrolyzer stack life	Hours	40,000	Assumed from
Per year stack degradation	%	1.5	Assumed
Operating time per year	hours	6,570	Assuming 75% CUF
Discount rate	%	6	Assumed
Salvage value of the investment	%	7.5	Assumed
Project lifetime	years	20	Assumed for electrochemical systems

References

1 B. Rutjens, K. von Foerster, B. Schmid, H. Weinrich, S. Sanz, H. Tempel and R.-A. Eichel, *Ind. Eng. Chem. Res.*, 2024, **63**, 3986–3996.
2 H. Yang, J. J. Kaczur, S. D. Sajjad and R. I. Masel, *J. CO2 Util.*, 2017, **20**, 208–217.
3 C. Xia, P. Zhu, Q. Jiang, Y. Pan, W. Liang, E. Stavitski, H. N. Alshareef and H. Wang, *Nat. Energy*, 2019, **4**, 776–785.
4 P. Deng, H. Wang, R. Qi, J. Zhu, S. Chen, F. Yang, L. Zhou, K. Qi, H. Liu and B. Y. Xia, *ACS Catal.*, 2020, **10**, 743–750.
5 D. Soo. Lee, *Anal. Chem.*, 1982, **54**, 1682–1686.
6 X. Chen, S. Chen, W. Huang, J. Zheng and Z. Li, *Electrochimica Acta*, 2009, **54**, 7370–7373.
7 E. V. Shkol'nikov, *Russ. J. Appl. Chem.*, 2010, **83**, 2121–2127.
8 T. Luo, S. Abdu and M. Wessling, *J. Membr. Sci.*, 2018, **555**, 429–454.
9 U. Nzotcha, S. Sanz, H. Tempel and R.-A. Eichel, *Angew. Chem. Int. Ed.*, 2025, **64**, e202418114.
10 M. Ramdin, B. De Mot, A. R. T. Morrison, T. Breugelmans, L. J. P. van den Broeke, J. P. M. Trusler, R. Kortlever, W. de Jong, O. A. Moultos, P. Xiao, P. A. Webley and T. J. H. Vlugt, *Ind. Eng. Chem. Res.*, 2021, **60**, 17862–17880.
11 M. Jouny, W. Luc and F. Jiao, *Ind. Eng. Chem. Res.*, 2018, **57**, 2165–2177.
12 M. Jouny, W. Luc and F. Jiao, *Ind. Eng. Chem. Res.*, 2018, **57**, 2165–2177.
13 N. T. Alwan, S. E. Shcheklein and O. M. Ali, *Case Stud. Therm. Eng.*, 2021, **27**, 101216.
14 Z. Liu, S. D. Sajjad, Y. Gao, J. Kaczur and R. Masel, *ECS Meet. Abstr.*, 2017, **MA2017-01**, 1413–1413.
15 J. J. Kaczur, H. Yang, Z. Liu, S. D. Sajjad and R. I. Masel, *Front. Chem.*, 2018, **6**, 1–16.